



# Experimental and Numerical Study on Crack-Arrest Behaviours of Rock-Like SCDC Specimens

Yao Song 

Received: 3 January 2020 / Accepted: 11 July 2020 / Published online: 17 July 2020  
© Springer Nature Switzerland AG 2020

**Abstract** Studying rock crack-arrest toughness, which determines the arrest behaviours in rock materials with cracks, is important to prevent further damage to rock mass. To investigate the crack-arrest behaviours both qualitatively and quantitatively, dynamic impact experiments (using caustics and photoelastic methods) were performed on rock-like (epoxy resin) single cleavage drilled compression (SCDC) specimens to study the crack-arrest behaviours and the microscopic fracture characteristics. The crack-arrest toughness of the SCDC specimen was obtained and the extended finite element method (XFEM) in ABAQUS software was used to validate the experimental results. The results show that under the interaction between reflected compression and tensile waves, the running crack experiences two crack-arrest periods before the final arrest, and the crack-arrest toughness stabilizes at a value of  $0.669 \text{ MPa m}^{1/2}$ . Moreover, the peak propagation velocity in each crack initiation process gradually decreases with the development of the crack path. Additionally, the observations by scanning electron microscopy (SEM) and photoelastic methods show that the roughness of the fracture surface is influenced by the crack-arrest behaviours, causing the spalling

fragments as well as wing micro-cracks in the fracture surface.

**Keywords** Rock dynamic fracture · Crack-arrest toughness · The dynamic caustic method · Numerical simulation · Scanning electron microscopy

## 1 Introduction

Rock fracture toughness is one of the most important mechanical parameters for rock material and can directly determine the fracture behaviours in rock mass (Zhang and Zhao 2014). Some serious disasters, such as earthquakes, landslides, and rock bursts, are mainly related to the initiation and development of micro-cracks in rock mass. Thus, the corresponding study of rock dynamic fracture behaviours is of great significance for practical engineering applications. In 2012, the International Society for Rock Mechanics (ISRM) Commission published the suggested method for the determination of the mode I fracture toughness for rock materials (Zhou et al. 2012). Various methods have been proposed for the determination of the fracture toughness of rock materials in recent years, including the use of cracked chevron notched Brazilian disc (CCNBD) (Fowell et al. 1995; Amrollahi et al. 2011; Wang et al. 2013; Dai et al. 2016; Wei et al. 2016a, b, 2017, 2018; Xu et al. 2016), cracked straight

---

Y. Song (✉)  
School of Traffic and Transportation Engineering, Dalian  
Jiaotong University, Dalian 116028, China  
e-mail: songyao\_1@126.com

through Brazilian disc (CSTBD) (Atkinson et al. 1982; Fowell and Xu 1994; Azar et al. 2015; Wang et al. 2016), notched semi-circular bend (NSCB) (Chen et al. 2009, 2016; Yin et al. 2012; Gao et al. 2015a, b; Kataoka et al. 2015; Yao et al. 2017) and cracked chevron notched semi-circular bend (CCNSCB) (Dai et al. 2011; Ayatollahi et al. 2016; Wei et al. 2016a, b) specimens. However, these types of specimens are mainly focused on the determination of the dynamic initiation and propagation fracture toughness due to the relatively limited dimensions. However, it is also important to investigate the crack-arrest behaviours of rock materials to prevent further damage to structural components with cracks (Yu and Yan 2008; Mahmoud and Dexter 2005). Therefore, single cleavage drilled compression (SCDC) (Grégoire et al. 2009; Yang et al. 2015) and single cleavage semi-circle compression (SCSC) (Wang et al. 2017a, b; Wang et al. 2015) specimens were proposed for the investigation of the complete cracking process of rock materials, including crack initiation, crack development and crack-arrest behaviours. Recently, Wang et al. (2017a, b) introduced the use of VB-SCSC specimens as a new method to study crack propagation and arrest behaviours.

However, even though recent studies on crack-arrest behaviours using SCDC and SCSC specimens are given in the corresponding references, the experimental results of the crack-arrest process are mostly based on qualitative analysis. There is still a lack of quantitative calculations and analyses of crack-arrest toughness for rock materials. Therefore, the caustic method was employed in this paper on the rock-like material (epoxy resin) as an effective approach for the determination of the fracture parameters in specimens due to its accuracy in data processing. The caustic method was first introduced by Manogg (1964) and has been extended to the field of fracture mechanics by researchers (Theocaris 1976; Kalthoff 1987; Semenski 1997). In the last few years, Yao et al. (2008), Yao and Xu (2011) studied the dynamic fracture behaviours in PMMA material with offset-parallel cracks and the crack initiation in graded material using the caustic method. Liu et al. (2016) introduced a new dynamic caustic digital array high-speed camera system and investigated mode I stress intensity factors in a PMMA cylindrical shell under a three-point-bend load. Yue et al. (2013) employed a dynamic caustic method and studied the interaction between a blast-induced crack

and double slit charge holes in PMMA specimens. In addition, the photoelastic method was also frequently employed to investigate the fracture behaviours of materials (Sanford and Dally 1979; Sanford 1989) and has been proven to be able to yield accurate results. Recently, Shimamoto et al. (2006) studied and compared the stress distributions and stress intensity factors around the crack tip under biaxial tensile stress conditions using both the photoelastic and thermoelectric methods. Hao et al. (2015) used the photoelastic method to explore the interactions between matrix cracks and inclusions of various shapes.

In this paper, epoxy resin was used as the experimental material to fabricate the SCDC specimen and simulate the cracking behaviours in rock mass. Using a high-speed camera, the caustic spots, and the isochromatic fringes around the crack tips at different moments were recorded. The dynamic stress intensity factors (DSIFs) were calculated and the crack-arrest toughness of the epoxy resin SCDC specimen was given. Meanwhile, a numerical method (XFEM) was used for the validation of experimental results and microscopic characteristics of epoxy resin SCDC were investigated using the SEM method.

## 2 The Dynamic Caustic Experiments

### 2.1 The Caustic Method

Figure 1 shows the formation of the caustic spot. The load on the specimen boundary would cause crack surface deformation. If the parallel light rays project to the front surface of the specimen, then the incident light paths transmitting through the crack surface would be changed, inducing a non-uniform light intensity distribution on the reference plane. There would be a shadow area (caustic spot) surrounded by a bright light loop (caustic curve) because of the divergence effect from the deformed crack surface and the consequence of light convergence. The stress intensity factor can then be calculated after the diameter of the caustic spot is determined. Figure 2 shows the characteristics of the mode I caustic spot around the crack tip.

Using a high-speed camera, the caustic patterns are clearly recorded at different moments during the cracking process. Thus, accurate transient positions of the crack tip and the corresponding crack length are

**Fig. 1** Formation of the caustic spot

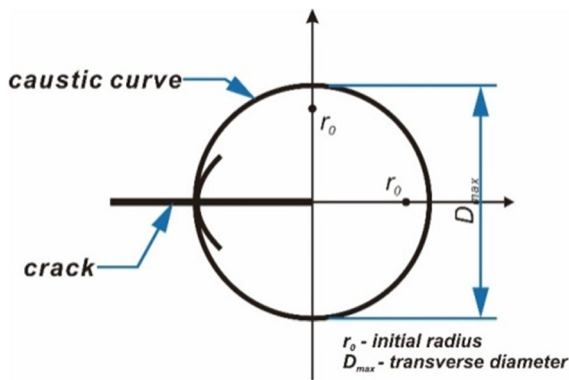
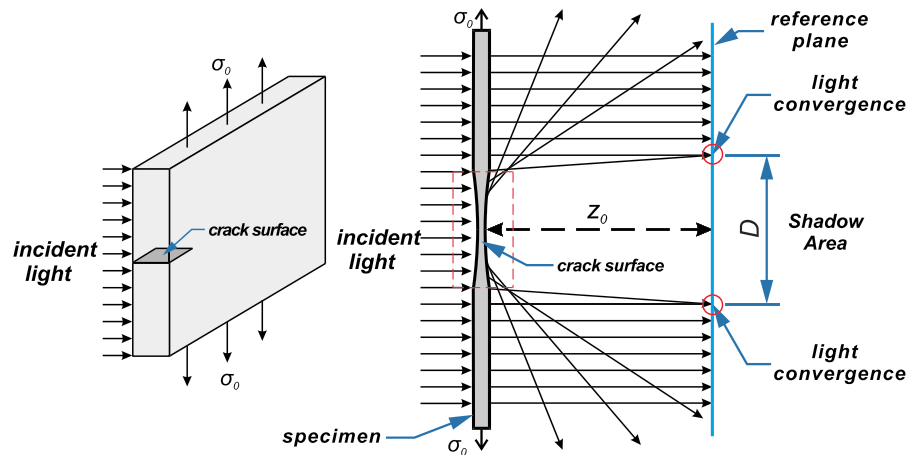


**Fig. 2** Mode I caustic spot

obtained. The crack propagation velocity can be expressed by the first derivative of the crack length with respect to time (Takahashi and Arakawa 1987):

$$c = \dot{l}(t) \tag{1}$$

The basic principle of the caustic method and the formation of the caustic spot are shown in Fig. 1. Based on the loading state and the boundary conditions of the SCDC specimen, it is considered that the mode-I fracture type is dominant for the complete cracking process. Given a point  $p(x,y)$  on the specimen plane, the corresponding point  $p'(x',y')$  on the reference plane can be given as (Papadopoulos 1992; Rosakis 1980)

$$r' = \lambda_m r - z_0 \text{grad} \Delta s(r, \theta) \tag{2}$$

where  $(r, \theta)$  and  $(r', \theta')$  represent the polar coordinates of point  $p$  and  $p'$  on the specimen and reference planes, respectively.  $\lambda_m$  denotes the optical enlargement factor

of the experimental system and equals 1 when the light source is parallel.  $\Delta s$  is the optical path difference. For a homogeneous linear elastic specimen under the plane stress condition,  $\Delta s$  can be given as follows:

$$\Delta s = 2d\eta \frac{K_I}{\sqrt{2\pi}} \cos \frac{\theta}{2} \tag{3}$$

where  $d$  is the thickness of the specimen,  $K_I$  is the mode I stress intensity factor, and  $\eta$  is the stress-optical constant of the specimen. Therefore, the dynamic stress intensity factor (DSIF) at the crack tip can be expressed in Eq. (4) based on Eq. (2), Eq. (3) and the crack propagation velocity (Rosakis 1980; Yue et al. 2017).

$$K_I^d = \frac{2\sqrt{2\pi}F(c)}{3(3.17)^{5/2}z_0\eta d\lambda_m^{3/2}} D^{5/2} \tag{4}$$

Here,  $Z_0$  is set to 900 mm in the experiment; The modification factor of the crack propagation velocity  $F(c)$ , which represents the effects of the crack velocity on the distribution of the dynamic stress field for a running crack, is given as follows:

$$F(c) = \frac{4\lambda_1\lambda_2 - (1 + \lambda_2^2)^2}{(1 + \lambda_2^2)(\lambda_1^2 - \lambda_2^2)} \tag{5}$$

$\lambda_1$  and  $\lambda_2$  are dimensionless coefficients related to the crack propagation velocity  $c$  and can be expressed as

$$\lambda_1 = \sqrt{1 - (c/c_1)^2}; \lambda_2 = \sqrt{1 - (c/c_2)^2} \tag{6}$$

where,  $c_1$  and  $c_2$  represent the longitudinal wave velocity and shear wave velocity, respectively. The value of  $F(c)$  is almost equal to 1 for practical crack velocities.

## 2.2 Experimental Setup

The digital dynamic caustic experimental system (Fig. 3) was employed in the experiments. This system mainly consists of a laser generator, a beam expander, two field lenses, a loading device and a high-speed camera with its corresponding computer. An infrared laser generator with wavelength of 532 nm and a maximum power of 300 mW was used as the light source during the test. To guarantee that the light beam was stable and clear, the power was set to 60 mW. The beam expander was used to transform the single light beam into conical barrel-type light so that it can be projected onto the field lens uniformly. Two field lenses with a diameter of 300 mm and a focal length of 900 mm were employed to ensure that parallel light passed through the specimen and that the light could converge on the imaging plane in the camera. The high-speed camera (brand: Photron, Japan; model: Fastcam-SA5-16G) was utilized to record the crack propagation process during the experiment. The frame rate was set to  $10^5$  fps to obtain a complete and clear field of view during the cracking process. The resolution was  $128 \times 352$ , and the length-to-pixel ratio was 1.8 mm/pixel.

## 2.3 Experimental Details

For the purpose of conducting both the caustic and photoelastic experiments with the same material, epoxy resin was utilized as the specimen material because of its unique birefringence under loading and transparency in the light path. The epoxy resin was first cast into a rectangular mould with dimensions of 400 mm\*300 mm\*4 mm (length\*width\*thickness). After 24 h of solidification and annealing (Fig. 4), the rectangular epoxy resin plank was cut into several SCDC specimens. The size of the specimen was 90 mm\*150 mm (length\*width), and the diameter of the drilled hole was 40 mm. A notch 9 mm in length and 1 mm in width was situated in each specimen, and a diamond saw was used to sharpen the front of the notch to form a pre-existing crack 1 mm in length and 0.2 mm in width. The dimensions of the SCDC specimen are shown in Fig. 5. The dynamic mechanical parameters of the epoxy resin are given in Table 1.

As shown in Fig. 6, a polymethyl methacrylate (PMMA) specimen with the same geometry as the SCDC specimen was first used as a model to adjust the supporting device to the best location before the formal experiments. A plate-type striker was used to provide surface impact loading. The dropping hammer was 3.85 kg, and the drop height was set to 400 mm.

## 2.4 Experimental Results and Analysis

Figure 7 shows the crack pattern of the specimen after the experiment. As shown in Fig. 7, the final crack path is almost a straight line perpendicular to the

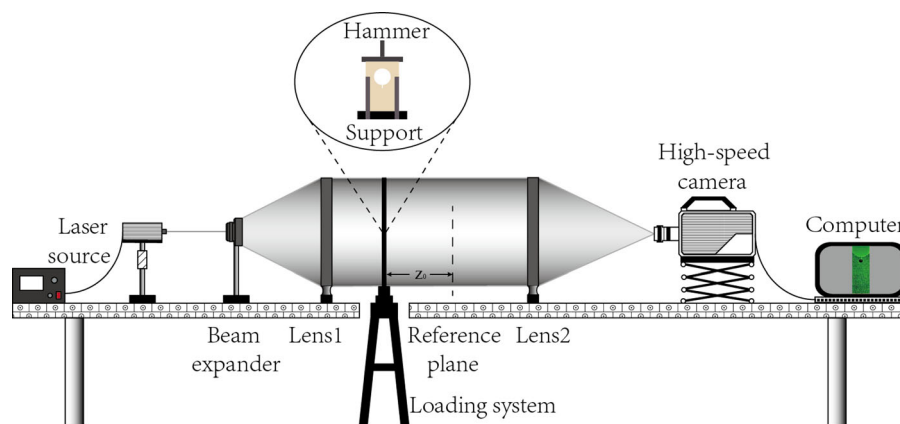


**Fig. 3** Digital dynamic caustic experimental system



**Fig. 4** The epoxy resin plank after solidification and annealing

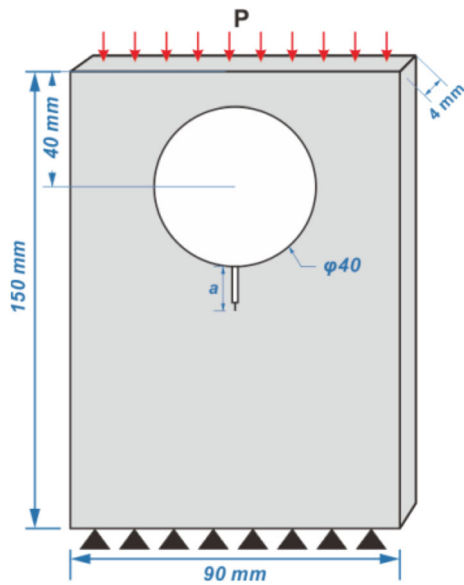


**Fig. 5** The SCDC specimen

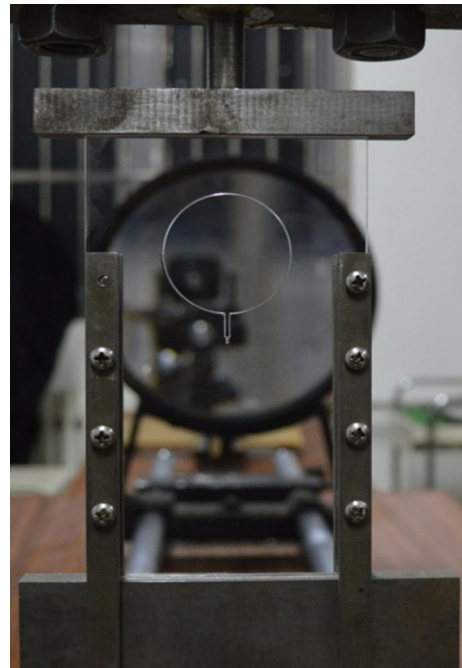


**Fig. 6** The loading device

crack tip, causing an unstable process of energy accumulation in the vicinity of the crack front. At the moment of 450  $\mu$ s, the diameter of the caustic spot reached the maximum value ( $D = 10.5$  mm), and then, the pre-existing crack began to initiate. Due to the sudden release of the elastic energy around the crack tip, the stress concentration level dropped rapidly, inducing the size of the caustic spot to shrink within a short time during the crack propagation from

**Table 1** The dynamic mechanical parameters of epoxy resin specimens

Parameters	$c_1$ (m/s)	$c_2$ (m/s)	$E_d$ (GPa)	$\nu$	$\eta$ ( $m^2/N$ )
Values	2347	1468	4.41	0.34	$0.85 \times 10^{-10}$

bottom edge of the specimen, which demonstrates that the opening mode (mode-I) fracture was dominant during the cracking process. Figures 8 and 9 show the series of the caustic spots around the crack tip and the spot diameters at different moments. As shown in Fig. 8 and Fig. 9, the size of the caustic spot fluctuates with intense amplitude during the period from 0  $\mu$ s to 450  $\mu$ s. This result illustrates that the stress wave generated by the impact continuously influenced the

460 to 520  $\mu$ s. At  $t = 520$   $\mu$ s, the reflected compression waves from the bottom edge of the SCDC specimen met the running crack front and forced it to stop propagating, causing the first crack arrest. The size of the caustic spot continued to decrease under the influence of the compression waves until  $t = 580$   $\mu$ s when the reflected tensile waves from both sides of the specimen acted on the front of the crack. The elastic energy began to accumulate again around the crack tip





**Fig. 7** Crack pattern after the experiment

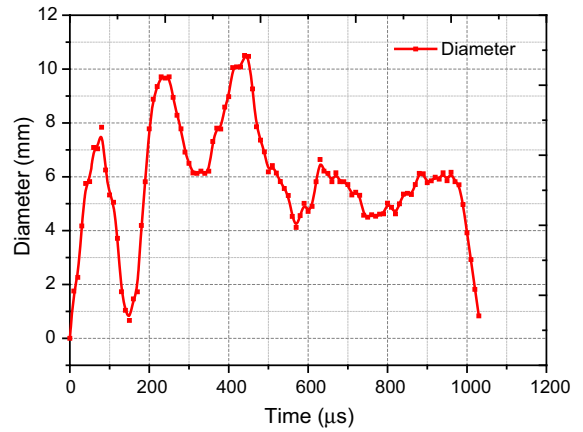


**Fig. 9** Evolution of the caustic spot diameter with time

and the diameter of the spot gradually increased. At  $t = 630 \mu s$ , the caustic spot diameter reached 6.64 mm, and the crack tip re-initiated. There was another crack arrest period (690 to 880  $\mu s$ ) before the crack completely stopped developing at  $t = 1010 \mu s$ . The change trend in the diameter of the caustic spot was similar to that in the first crack arrest period.

Figure 10 shows the change in the crack propagation velocity with time. At  $t = 450 \mu s$  when the pre-

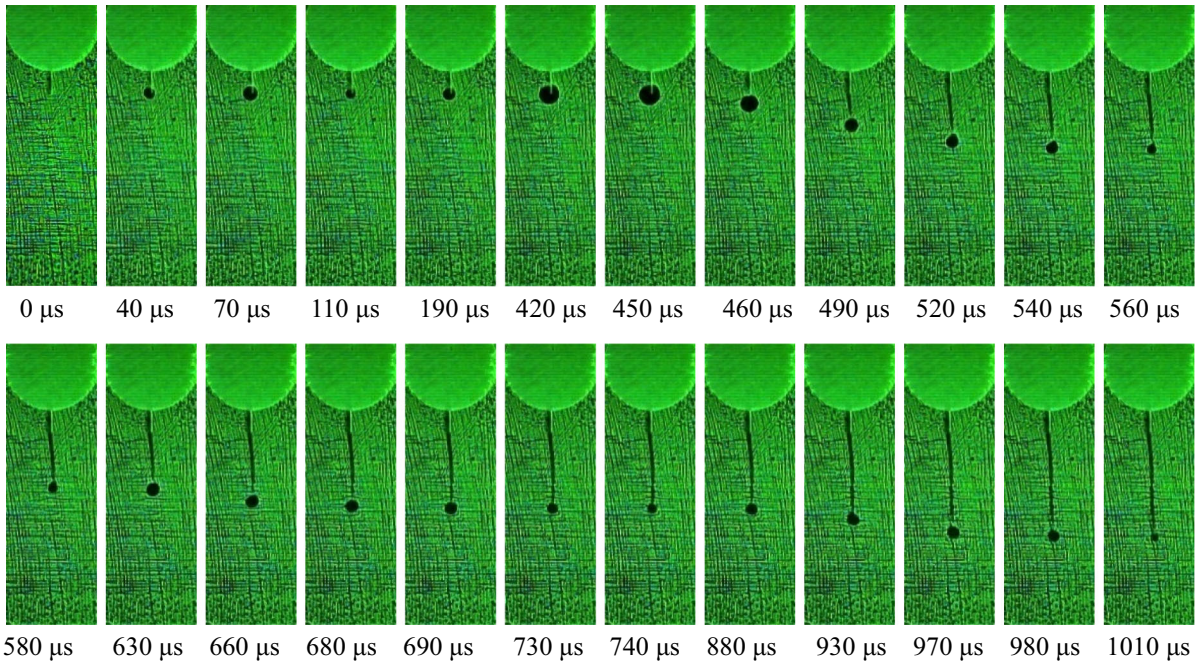


**Fig. 8** Series of caustic spots around the crack tip

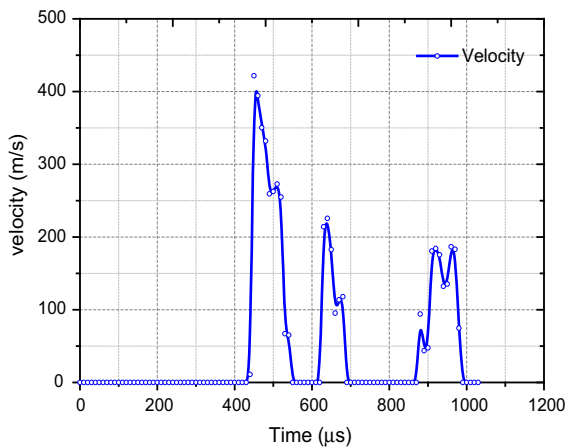


**Fig. 10** Evolution of the crack propagation velocity with time

existing crack first initiated, the crack propagation velocity rapidly reached the maximum value of 421.76 m/s due to the sudden energy release from the crack tip. Under the influence of the compression wave from the bottom edge of the specimen, the crack propagation velocity decreased in the short period before the first crack arrest. At  $t = 630 \mu\text{s}$  when the crack re-initiated, the propagation velocity first reached the second peak value of 225.57 m/s and then declined within 40  $\mu\text{s}$ . When  $t = 880 \mu\text{s}$ , the crack tip was subjected to the final initiation, and the third peak value of the propagation velocity was 184.27 m/s. It was evident that the peak value of the crack propagation velocity during the three initiation processes gradually decreased. This can be explained by the fact that the driving energy for fracture steadily dissipated with the development of the crack. Thus, the peak value that the crack velocity could reach after its re-initiation was lower than the value that it could reach previously. Figure 10 shows that the velocity change trends in the first two cracking processes were quite similar to each other, while a velocity change curve with multiple fluctuations was found in the final cracking process. This could be explained as a size effect of the specimen in that the propagating crack was influenced by the reflected waves more severely as it approached to the bottom edge of the specimen. Therefore, the variation of the crack propagation velocity was less stable than before.

Figure 11 shows the time evolution of the DSIF and crack length during the cracking process. During the period between 0 and 430  $\mu\text{s}$ , the pre-existing crack

did not initiate, and the DSIF continued rising with intense fluctuations, indicating that the crack tip constantly absorbed the elastic energy for the purpose of initiation. At the moment of 440  $\mu\text{s}$  when the DSIF achieved the critical value of  $2.93 \text{ MPa m}^{1/2}$ , the pre-existing crack initiated, and then, the DSIF exhibited a sudden decrease due to the reduction of the stress concentration level around the crack tip. Correspondingly, the crack developed promptly from 0 mm at 440  $\mu\text{s}$  to 23.69 mm at 520  $\mu\text{s}$ . At  $t = 530 \mu\text{s}$ , the DSIF reduced to  $0.671 \text{ MPa m}^{1/2}$ , and the first period of crack arrest appeared. The value of the DSIF decreased because of the influence from the reflected compression wave on the crack tip to  $K_I^d = 0.282 \text{ MPa m}^{1/2}$  at  $t = 570 \mu\text{s}$ . Afterwards, the energy around the crack tip began to be accumulated again under the action from the tensile stress waves, causing the DSIF value to rise again. The crack length remained at approximately 27.5 mm during the corresponding period (530  $\mu\text{s}$  to 620  $\mu\text{s}$ ). When  $t = 630 \mu\text{s}$ , the DSIF  $K_I^d$  reached  $0.932 \text{ MPa m}^{1/2}$ , causing a re-initiation of the crack front. Similarly, the running crack was subjected to another crack-arrest period (2nd crack arrest in Fig. 11) before it completely stopped developing in the end at  $t = 1030 \mu\text{s}$ . The total crack propagation length was 52.5 mm. The coordinates of the three crack-arrest points are marked on the  $K_I^d$ - $t$  curve in Fig. 11. The values of the DSIFs at the crack-arrest moments were very close to each other ( $0.671 \text{ MPa m}^{1/2}$ ,  $0.668 \text{ MPa m}^{1/2}$ , and  $0.668 \text{ MPa m}^{1/2}$ ). Therefore, the average of the three DSIF values above could be used as the crack-arrest fracture toughness for epoxy resin SCDC specimens. Namely, the crack-arrest fracture toughness  $K_I^a = 0.669 \text{ MPa m}^{1/2}$ . In addition, the 2nd crack arrest period was longer than the 1st period (100  $\mu\text{s}$  for the first crack arrest period; 190  $\mu\text{s}$  for the second crack arrest period). This was because the energy supply for fracture gradually dissipated with the development of the crack length. Therefore, the second re-initiation required more time than the first initiation. It was also interesting to note that the initiation fracture toughness of pre-existing cracks was much higher than that in the re-initiation situations. This was because the pre-existing crack was manually fabricated, causing the crack front not to be as sharp as the propagating crack. Consequently, the intense stress

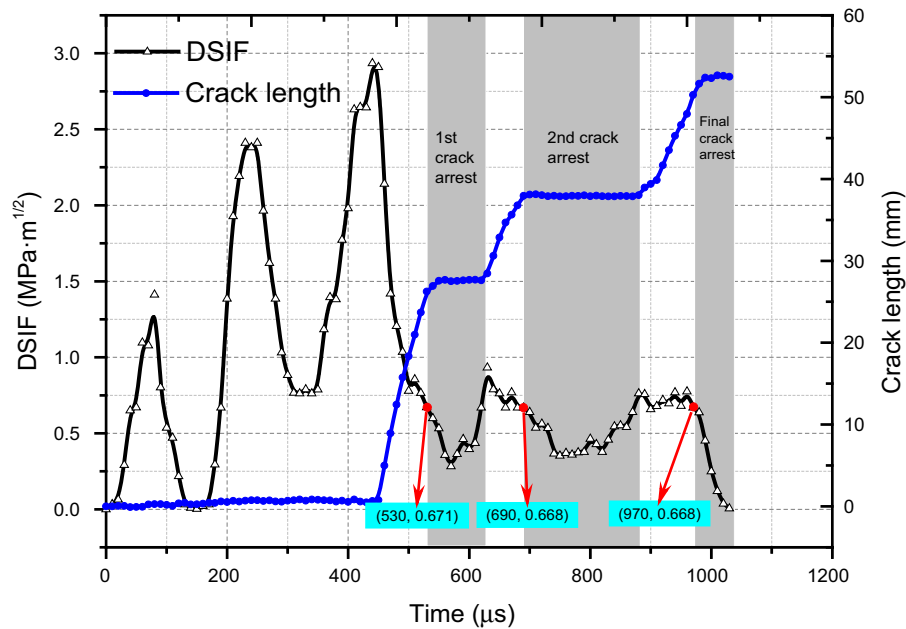


**Fig. 11** Evolution of the DSIF and crack length with time

concentration around the pre-existing crack raised the critical DSIF value for initiation.

## 2.5 Numerical Method for Validation of the Experimental Results

For the purpose of validating of the experimental results in Fig. 11, a numerical model was used to simulate the cracking behaviours and to calculate the DSIFs in the SCDC specimen by employing the enhanced extended finite element method (XFEM) in ABAQUS software.

Figure 12 shows the geometry of the numerical model and the typical mesh for the SCDC specimen. The size parameters of the numerical model were equal to those of the SCDC specimens in the experiments, and a typical XFEM crack 10 mm in length was set to represent the pre-existing crack. The bottom edge of the numerical model was fixed in rotation and along the Y-axis. The bottom surface of the hammer and top surface of the specimen model were set as master and slave surfaces, respectively. The hard contact and frictionless mode was set as the contact properties between the hammer and specimen. The numerical model consisted of 1378 four-node bilinear plane stress quadrilateral elements and the meshes were optimized around the circular hole and

the XFEM crack. The average element size around the circular hole was approximately 0.47 mm in arc length. The mechanical parameters employed in the simulation model were strictly consistent with those of SCDC specimens used in experiments.

The dynamic stress intensity factor at the crack tip can be obtained using the integral  $I^{int}$ , which is determined by the J-domain in the vicinity of the crack tip. The DSIF can then be given as [50],

$$K_1^d = \frac{E_d}{2(1 - \nu^2)f_1(\dot{l})} I^{int} \quad (7)$$

where  $l$  denotes the crack length during the fracture process in the SCDC specimen and  $f_1(\dot{l})$  denotes a universal function with respect to the crack propagation velocity  $\dot{l}$ . The path independence of the numerical DSIF values was checked to guarantee the accuracy of the calculation results. This can be realized by performing calculations of the J-integral on various contours with different distances from the crack tip. As shown in Fig. 13, a complete crack path was given by the numerical model, and a series of variations in the von Mises stress field was obtained during the fracture process. The characteristics of the crack paths in both the experiments and simulations are similar. Figure 14 shows the DSIFs calculated



**Fig. 12** Geometry of the numerical model and typical mesh for the SCDC model

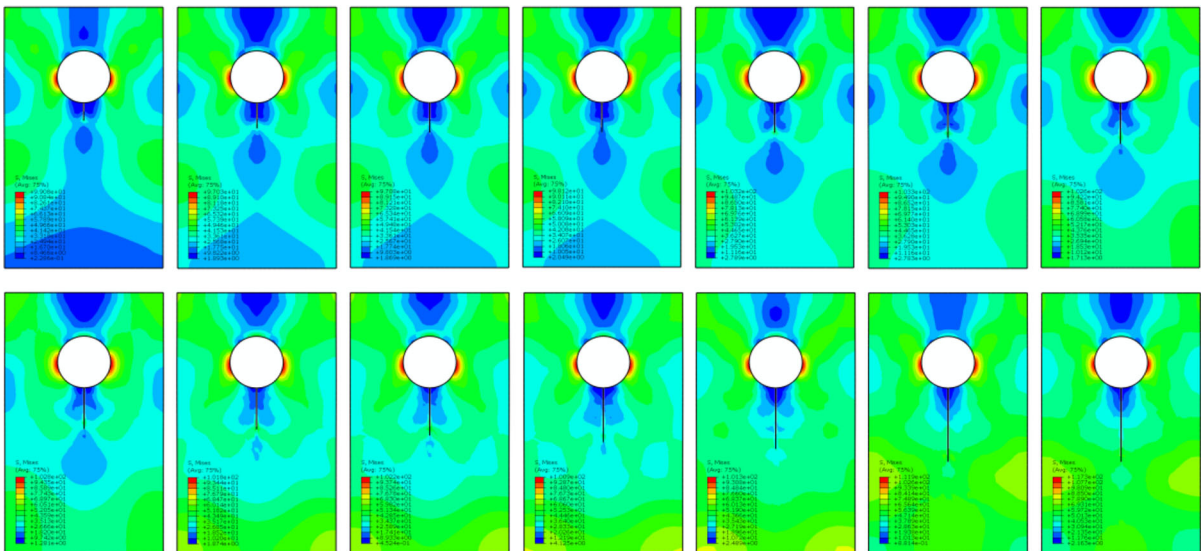
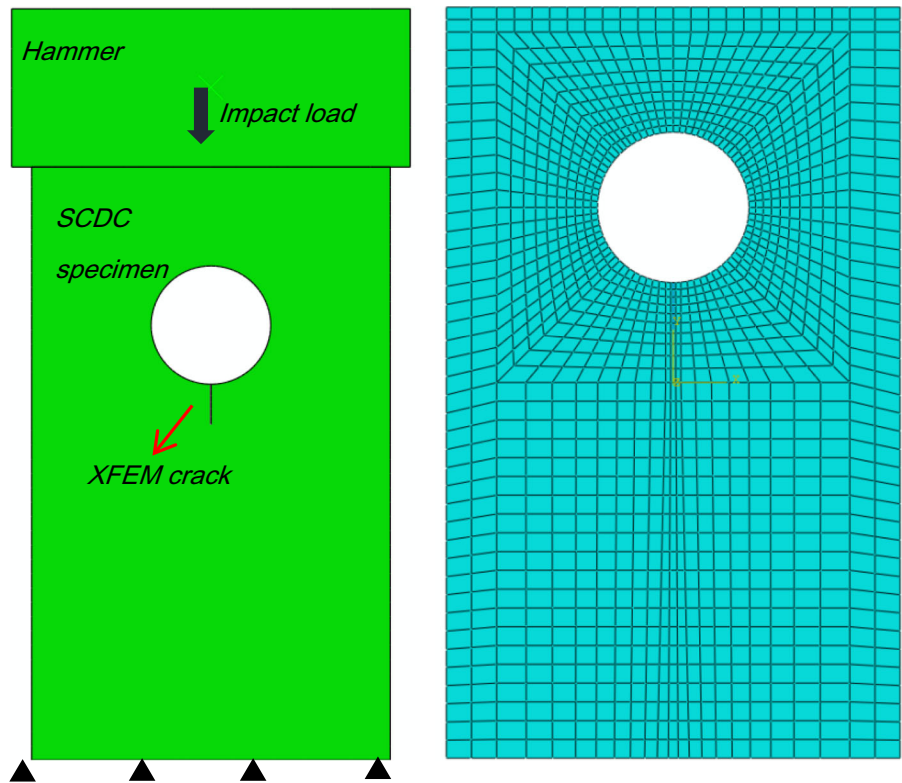


**Fig. 13** von Mises stress field of the simulation result

from the numerical simulation using XFEM and from the caustic experiments during the cracking process. The comparison results in Fig. 14 show good agreement. The maximum difference in DSIF values

between the caustic and simulation results is approximately 12.74%.

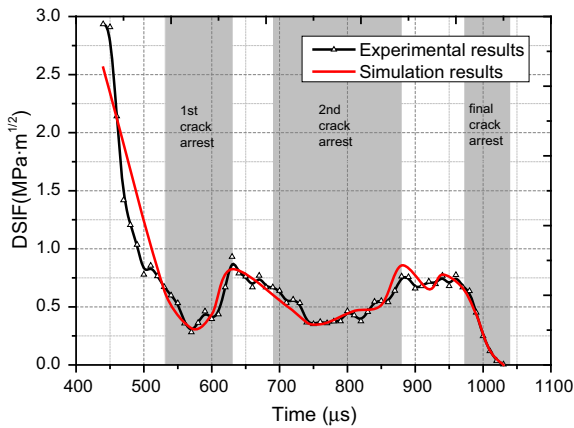


**Fig. 14** Comparison of DSIF values for SCDC specimens during the cracking process

### 3 Microscopic Fracture Characterization of SCDC Specimens

Using the scanning electron microscopy (SEM), micrographs of the fracture surface were obtained for microscopic fracture characterization of SCDC specimens. As shown in Fig. 15, three parts (P1, P2 and P3) along the crack path were chosen for the SEM tests. The geometric dimensions of the chosen parts were controlled within a rectangular block of 2 mm\*1 mm\*4 mm in length\*width\*thickness, and

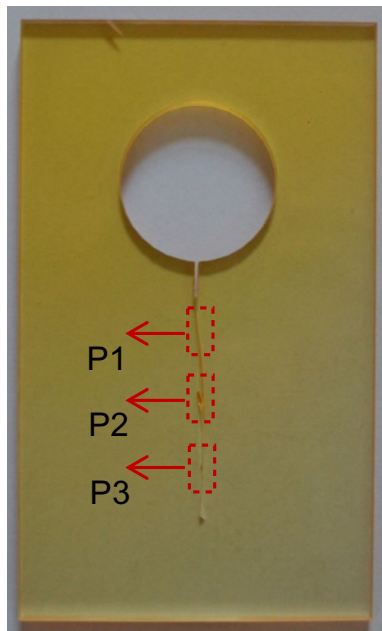


**Fig. 15** Three parts along the crack path in the SCDC specimen

the fracture surface of the samples was coated with gold for 20 min. The enlargement factors of SEM were set to 200, 500 and 1000 for each part. Figure 16 shows that the roughness varies along the crack path and is strongly influenced by the compression and reflection waves in the specimen. In the P1 block, the fracture surface is rather smooth and continuous when the pre-existing crack initially starts to develop. In the P2 block, where the running crack first ceased developing, the fracture surface is clearly coarser than that in the P1 block due to the influence of the reflected compression wave propagating from the bottom of the specimen. Meanwhile, some spalt fragments and wing micro-cracks can be observed in P2. This phenomenon is related to the tension effect of the reflected waves from both sides of the specimen, causing micro-cracks in the fracture surface to initiate and develop. Microscopic fracture characteristics similar to those in the P2 block can also be found in the P3 block, where the crack stopped propagating for a second time. The only difference is that the quantity of spalling fragments is lower than that found in the P2 block. This is related to the lower elastic energy in the compression and reflection waves during this cracking period.

### 4 Discussion and Conclusions

For further validation and investigation of the experimental and numerical results, a dynamic photoelastic experiment was performed on another epoxy resin SCDC specimen to reveal the fracture mechanism in the SCDC specimen. The cracking process recorded by the high speed camera in the dynamic photoelastic experiment is shown in Fig. 17. When the pre-existing crack initiates at  $t = 100 \mu\text{s}$ , the state of the isochromatic fringes show typical butterfly fringes around the crack tip. Then, the running crack experiences the first crack-arrest period (660  $\mu\text{s}$  and 700  $\mu\text{s}$  in Fig. 17). Clearly, the crack-arrest behaviour is mainly related to the interaction between reflected compression and tensile waves around the crack tip. Combined with the analysis in Sect. 3, the influence from the reflected compression waves is the reason why the fracture surface becomes coarse in the crack-arrest area, while the tensile waves mainly account for the existence of the spalling fragments and wing micro-cracks. In addition, such superposition and interactions between compression and tensile waves change the stress state

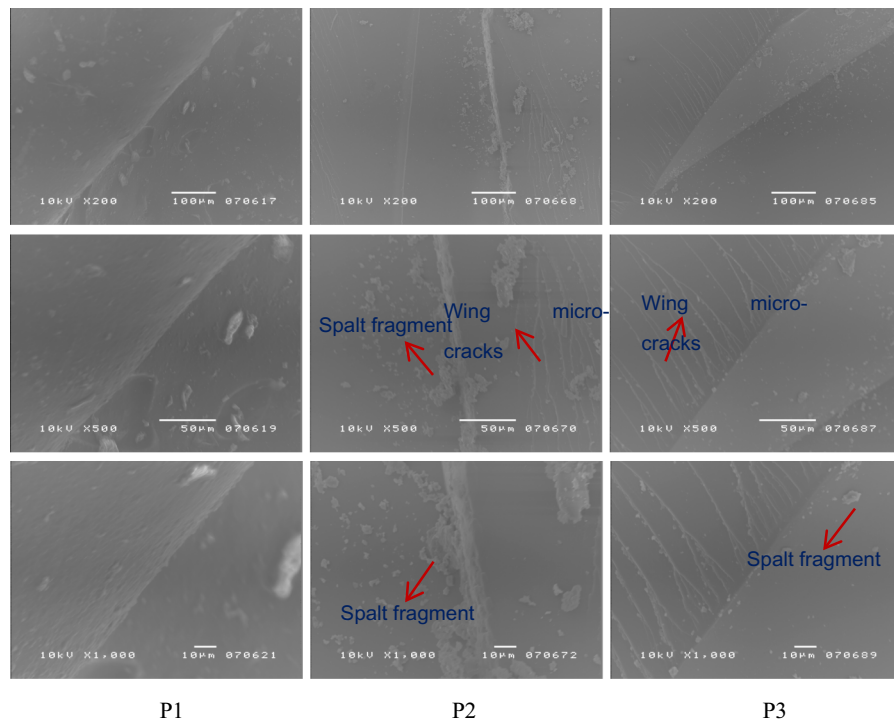


**Fig. 16** Typical SEM images of the fracture surface in the three parts with enlargements of 200, 500 and 1000

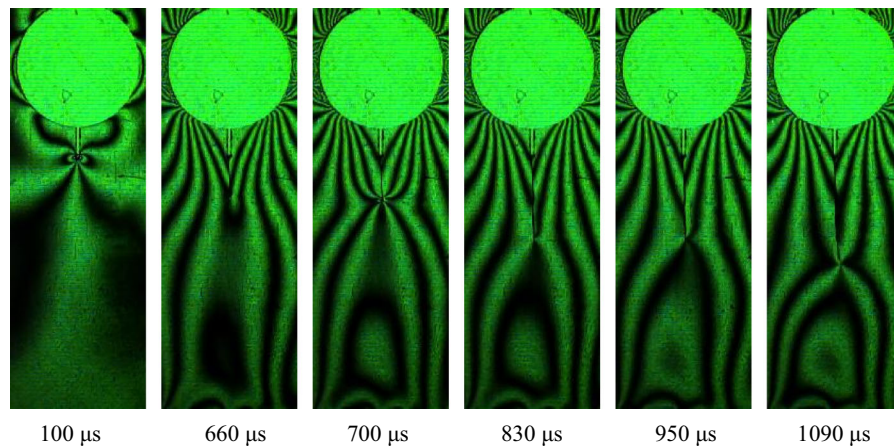


**Fig. 17** Typical photoelastic results for the cracking process in the epoxy resin SCDC specimen

in the SCDC specimen, causing the redistribution of the stress field in the vicinity of the crack tip. The elastic energy is re-accumulated at the crack tip for re-initiation. Before the final arrest of the crack path at  $t = 1090 \mu s$ , the situation in the second crack-arrest period (830  $\mu s$  and 950  $\mu s$  in Fig. 17) is very similar to that in the first.

In this paper, the experimental methods (caustics, SEM and photoelasticity) were employed to study the crack-arrest behaviour and the microscopic fracture characteristics of the epoxy resin SCDC specimen. Meanwhile, the XFEM in ABAQUS software was used for the purpose of validating the experimental results. The key conclusions are as follows:

(1) The peak propagation velocity in each crack initiation process gradually decreases with the development of the crack path. In addition, in the final cracking process, the crack propagation velocity changes with multiple fluctuations due to the size effect of the SCDC specimen.

(2) The crack in the SCDC specimen experiences two crack-arrest periods before the final arrest in crack development. The crack-arrest toughness stabilizes at a certain value of  $0.669 \text{ MPa m}^{1/2}$ . In addition, the second crack-arrest period is longer than the first due to the dissipation in energy for crack initiation.

(3) The roughness of the fracture surface in the SCDC specimen varies along the crack path. Spall fragments and wing micro-cracks caused by the interactions between reflected compression and tensile waves exist during the crack-arrest period.

**Acknowledgements** This work was supported by National Natural Science Foundation of China (Grant Number: 51974318). The author also thanks the reviewers and journal editorial of Geotechnical and Geological Engineering.

## References

- Amrollahi H, Baghbanan A, Hashemolhosseini H (2011) Measuring fracture toughness of crystalline marbles under modes I and II and mixed mode I-II loading conditions using CCNBD and HCCD specimens. *Int J Rock Mech Min Sci* 48(7):1123–1134
- Atkinson C, Smelser RE, Sanchez J (1982) Combined mode fracture via the cracked Brazilian disk test. *Int J Fract* 18(4):279–291
- Ayatollahi MR, Mahdavi E, Alborzi MJ, Obara Y (2016) Stress intensity factors of semi-circular bend specimens with straight-through and chevron notches. *Rock Mech Rock Eng* 49(4):1161–1172
- Azar HF, Choupani N, Afshin H, Moghadam RH (2015) Effect of mineral admixtures on the mixed-mode (I/II) fracture characterization of cement mortar: CTS, CSTBD and SCB specimens. *Eng Fract Mech* 134:20–34
- Chen R, Xia K, Dai F, Lu F, Luo SN (2009) Determination of dynamic fracture parameters using a semi-circular bend technique in split Hopkinson pressure bar testing. *Eng Fract Mech* 76(9):1268–1276
- Chen R, Li K, Xia K, Lin Y, Yao W, Lu F (2016) Dynamic fracture properties of rocks subjected to static pre-load using notched semi-circular bend method. *Rock Mech Rock Eng* 49(10):3865–3872
- Dai F, Xia K, Zheng H, Wang YX (2011) Determination of dynamic rock mode-I fracture parameters using cracked chevron notched semi-circular bend specimen. *Eng Fract Mech* 78(15):2633–2644
- Dai F, Xu Y, Zhao T, Xu NW, Liu Y (2016) Loading-rate-dependent progressive fracturing of cracked chevron-notched Brazilian disc specimens in split Hopkinson pressure bar tests. *Int J Rock Mech Min Sci* 88:49–60
- Fowell RJ, Xu C (1994) The use of the cracked Brazilian disc geometry for rock fracture investigations. *Int J Rock Mech Min Sci Geomech* 31(6):571–579
- Fowell RJ, Hudson JA, Xu C, Hao X (1995) Suggested method for determining mode I fracture toughness using cracked chevron notched Brazilian disc (CCNBD) specimens. *Int J Rock Mech Min Sci Geomech* 7(32):322A
- Gao G, Yao W, Xia K, Li Z (2015a) Investigation of the rate dependence of fracture propagation in rocks using digital image correlation (DIC) method. *Eng Fract Mech* 138:146–155
- Gao G, Huang S, Xia K, Li Z (2015b) Application of digital image correlation (DIC) in dynamic notched semi-circular bend (NSCB) tests. *Exp Mech* 55(1):95–104
- Grégoire D, Maigre H, Combescure A (2009) New experimental and numerical techniques to study the arrest and the restart of a crack under impact in transparent materials. *Int J Solids Struct* 46(18–19):3480–3491
- Hao W, Tang C, Yuan Y, Ma Y (2015) Photoelastic investigation of interaction between matrix crack and different shapes of inclusions. *J Test Eval* 44(6):2352–2360
- Kalthoff JF (1987) The shadow optical method of caustics. In: *Static and dynamic photoelasticity and caustics*. pp 407–522
- Kataoka M, Obara Y, Kuruppu M (2015) Estimation of fracture toughness of anisotropic rocks by semi-circular bend (SCB) tests under water vapor pressure. *Rock Mech Rock Eng* 48(4):1353–1367
- Liu W, Wang S, Yao X (2016) Experimental study on stress intensity factor for an axial crack in a PMMA cylindrical shell. *Polym Test* 56:36–44
- Mahmoud HN, Dexter RJ (2005) Propagation rate of large cracks in stiffened panels under tension loading. *Mar Struct* 18(3):265–288
- Manogg P (1964) Schattenoptische Messung der spezifischen Bruchenergie während des Bruchvorgangs bei Plexiglas. *Proc Int Con Phys Non Cryst Solids* 481–490
- Papadopoulos GA (1992) *Fracture mechanics. The experimental method of caustics and the det.-criterion of fracture*. Springer, Berlin, pp 134–204
- Rosakis AJ (1980) Analysis of the optical method of caustics for dynamic crack propagation. *Eng Fract Mech* 13(2):331–347
- Sanford RJ (1989) Determining fracture parameters with full-field optical methods. *Exp Mech* 29(3):241–247
- Sanford RJ, Dally JW (1979) A general method for determining mixed-mode stress intensity factors from isochromatic fringe patterns. *Eng Fract Mech* 11(4):621–633
- Seminski D (1997) Method of caustics in fracture mechanics of mechanically anisotropic materials. *Eng Fract Mech* 58(1–2):1–10
- Shimamoto A, Ohkawara H, Zhao HY (2006) Evaluation of stress intensity factors in biaxial tensile stress using thermalelasticity and photoelasticity. *Key Eng Mater* 2006(324):1103–1108

- Takahashi K, Arakawa K (1987) Dependence of crack acceleration on the dynamic stress-intensity factor in polymers. *Exp Mech* 27(2):195–199
- Theocaris PS (1976) Stress concentrations in anisotropic plates by the method of caustics. *J Strain Anal Eng Des* 11(3):154–160
- Wang QZ, Fan H, Gou XP, Zhang S (2013) Recalibration and clarification of the formula applied to the ISRM-suggested CCNBD specimens for testing rock fracture toughness. *Rock Mech Rock Eng* 46(2):303–313
- Wang M, Zhu Z, Xie J (2015) Experimental and numerical studies of the mixed-mode I and II crack propagation under dynamic loading using SHPB. *Chin J Rock Mech Eng* 34(12):2474–2485 [in Chinese]
- Wang QZ, Yang JR, Zhang CG, Zhou Y, Li L, Wu LZ, Huang RQ (2016) Determination of dynamic crack initiation and propagation toughness of a rock using a hybrid experimental-numerical approach. *J Eng Mech* 142(12):04016097
- Wang X, Zhu Z, Wang M, Ying P, Zhou L, Dong Y (2017a) Study of rock dynamic fracture toughness by using VB-SCSC specimens under medium-low speed impacts. *Eng Fract Mech* 181:52–64
- Wang M, Zhu Z, Dong Y, Zhou L (2017b) Study of mixed-mode I/II fractures using single cleavage semicircle compression specimens under impacting loads. *Eng Fract Mech* 177:33–44
- Wei MD, Dai F, Xu NW, Zhao T (2016a) Stress intensity factors and fracture process zones of ISRM-suggested chevron notched specimens for mode I fracture toughness testing of rocks. *Eng Fract Mech* 168:174–189
- Wei MD, Dai F, Xu NW, Liu JF, Xu Y (2016b) Experimental and numerical study on the cracked chevron notched semi-circular bend method for characterizing the mode I fracture toughness of rocks. *Rock Mech Rock Eng* 49(5):1595–1609
- Wei MD, Dai F, Liu Y, Xu NW, Zhao T (2017) An experimental and theoretical comparison of CCNBD and CCNSCB specimens for determining mode I fracture toughness of rocks. *Fatigue Fract Eng Mater Struct* 41(5):1002–1018
- Wei MD, Dai F, Xu NW, Zhao T (2018) Experimental and numerical investigation of cracked chevron notched Brazilian disc specimen for fracture toughness testing of rock. *Fatigue Fract Eng Mater Struct* 41(1):197–211
- Xu Y, Dai F, Zhao T, Xu NW, Liu Y (2016) Fracture toughness determination of cracked chevron notched Brazilian disc rock specimen via Griffith energy criterion incorporating realistic fracture profiles. *Rock Mech Rock Eng* 49(8):3083–3093
- Yang JR, Zhang CG, Zhou Y, Zhu ZM, Wang QZ (2015) A new method for determining dynamic fracture toughness of rock using SCDC specimens. *Chin J Rock Mech Eng* 34(2):279–292 [in Chinese]
- Yao XF, Xu W (2011) Recent application of caustics on experimental dynamic fracture studies. *Fatigue Fract Eng Mater Struct* 34(6):448–459
- Yao XF, Xu W, Bai SL, Yeh HY (2008) Caustics analysis of the crack initiation and propagation of graded materials. *Compos Sci Technol* 68(3):953–962
- Yao W, Xu Y, Liu HW, Xia K (2017) Quantification of thermally induced damage and its effect on dynamic fracture toughness of two mortars. *Eng Fract Mech* 169:74–88
- Yin T, Li X, Xia K, Huang S (2012) Effect of thermal treatment on the dynamic fracture toughness of Laurentian granite. *Rock Mech Rock Eng* 45(6):1087–1094
- Yu JL, Yan XQ (2008) Analysis on crack arrest performance of crack-stiffened panel. *Petro Chem Equip* 5:005
- Yue ZW, Yang LY, Wang YB (2013) Experimental study of crack propagation in polymethyl methacrylate material with double holes under the directional controlled blasting. *Fatigue Fract Eng Mater Struct* 36(8):827–833
- Yue Z, Song Y, Yang R, Yu Q (2017) Comparison of caustics and the strain gage method for measuring mode I stress intensity factor of PMMA material. *Polym Test* 59:10–19
- Zhang QB, Zhao J (2014) A review of dynamic experimental techniques and mechanical behaviour of rock materials. *Rock Mech Rock Eng* 47(4):1411–1478
- Zhou YX, Xia KW, Li XB, Li HB, Ma GW, Zhao J, Zhou ZL, Dai F (2012) Suggested methods for determining the dynamic strength parameters and mode-I fracture toughness of rock materials. *Int J Rock Mech Min Sci* 49:105–112

**Publisher's Note** Springer Nature remains neutral with regard to jurisdictional claims in published maps and institutional affiliations.